

The X-ray Telescope (XRT) for the Solar-B Mission

L. Golub[†], G. Austin, J. Bookbinder, D. Caldwell, P. Cheimets, J. Cirtain, M. Cosmo, E. DeLuca, P. Reid, A. Sette, M. Weber, T. Sakao, R. Kano, K. Shibasaki, J. McCracken, J. Carpenter, H. Haight, R. Siler, E. Wright, J. Tucker, H. Rutledge, M. Barbera, G. Peres and S. Varisco

Received: date

Abstract.

The X-ray Telescope (XRT) of the Solar-B mission will provide an unprecedented combination of spatial and temporal resolution in solar coronal studies. The high sensitivity and broad dynamic range of XRT, coupled with the spacecraft's onboard memory capacity and the planned downlink capability will permit a broad range of coronal studies over an extended period of time, for targets ranging from quiet Sun to X-flares. This paper discusses in detail the design, calibration and measured performance of the XRT instrument up to the focal plane. The CCD camera and data handling are discussed separately in a companion paper.

Keywords: Sun: corona Sun: X-rays Sun: MHD

1. Introduction to XRT and Solar-B

The solar outer atmosphere presents a unique set of problems for the observer: the temperature varies from 5800 K to more than 10^7 K, with a consequent range in primary emission wavelengths; the target has a large angular size while much of the relevant physics takes place on very small spatial scales; the aspect of most interest, the variability of the atmosphere, is due to the presence of strong and intermittent magnetic fields rooted in the photosphere. The **B**-field traverses a broad temperature regime from the visible surface to the corona. The wavelengths which need to be observed cover a comparable

[†] Harvard-Smithsonian Center for Astrophysics
60 Garden Street
Cambridge MA 02138
Tel.: +1-617-495-7177
Fax: +1-617-496-7577
(lgolub@cfa.harvard.edu)

J-side Group
JAXA/ISAS

MSFC Group
ASRI Huntsville

Palermo Group
Osservatorio Astronomico "G. S. Vaiana"



© 2006 Kluwer Academic Publishers. Printed in the Netherlands.

range, from visible to X-ray, while the spatial scales which need to be resolved range from a fraction of an arcsecond at the surface to $> 10^5$ km in the corona; the time scales which need to be studied range from microseconds to years (Golub, 2003). The combination of instruments chosen for the Solar-B mission has been selected with these considerations in mind.

2. Brief Science Overview

Because the solar outer atmosphere is at a temperature of several million Kelvins (MK) its primary emission is in the soft X-ray spectral range. X-ray images display the spatial distribution of this high-temperature plasma, and diagnostics are available to determine the distribution as a function of temperature of the coronal material. The X-ray Telescope (XRT) will provide an unprecedented combination of spatial, spectral and temporal coverage, which will allow a broad range of scientific investigations to be carried out, as listed in Table I. In addition to the inherent capabilities of the XRT, the spectral data provided by EIS and spectroheliograms and the **B** measurements from SOT/FPP will greatly extend our analytic capability in studies of the structure and dynamics of the solar atmosphere.

Table I. Scientific Objectives of the XRT

Objective	Representative Questions
1. Coronal Mass Ejections	How are they triggered? What is relation to B structure? What is relation between large-scale instabilities and dynamics of fine structure?
2. Coronal Heating.	How do coronal structures brighten? Are there waves, and do they correlate with brightness? Do loop-loop interactions cause significant heating?
3. Reconnection and Jets	Where and how does reconnection occur in the corona? What is its relation to B ?
4. Flare Energetics.	Same as 1. above.
5. Photosphere-Corona Coupling	Can a direct connection between coronal and photospheric events be established? How is energy transferred to the corona? What determines coronal transverse fine structure?

The XRT will provide several "firsts" in capability in comparison with previous X-ray imagers. Some of these are summarized below, and further details are presented in DeLuca *et al.* (2005).

- Unprecedented combination of spatial resolution, field of view and image cadence.
- Broadest temperature coverage of any coronal imager to date.
- High data rate for observing rapid changes in topology and temperature.
- Extremely large dynamic range to detect corona from coronal holes to X-flares.
- Flare buffer, onboard storage and high downlink rate provide unique observing capability.

2.1. INSTRUMENT FLOWDOWN REQUIREMENTS

The scientific objectives which have been specified for the XRT lead to a set of flowdown requirements, as shown in Table II. These are the minimum performance requirements needed to meet the objectives; in most cases the as-built XRT exceeds these requirements, as will be discussed below.

These requirements lead to the choice of a grazing-incidence (GI) X-ray telescope, with a design chosen to meet the specific requirements. We note that the XRT design provides image quality in the central portion of the field which is consistent with the manufacturing tolerances. The design and fabrication of the XRT are discussed in detail in Sec. 3.1.

XRT Temperature Sensitivity. Requirements 3. and 4. in Table II may be singled out as involving more of the telescope design elements simultaneously than any of the other requirements. There are a number of factors involved in determining the temperature range of a GI telescope, and additional factors determine the temperature sensitivity. Design elements include: the reflectance of the telescope as a function of incoming photon energy E ; the transmission of the entrance aperture prefilters as a $f(E)$; the transmission of the focal plane analysis filters as a $f(E)$; and the response of the focal plane detector as $f(E)$. We see that each of the major subsystems of the XRT contributes to this requirement.

In the following sections we first discuss the major subassemblies of the XRT separately. The overall temperature response and temperature discrimination of the XRT is discussed subsequently.

3. Major Subsystems

The components of the XRT are shown schematically in Fig. 1. The XRT is, in principle, a simple instrument: a grazing incidence optic focuses solar

Table II. Instrument Flowdown Requirements

Requirement	Definition	Required Value
1. Exposure time	Shutter-open time	4ms – 10 s
2. Cadence	Time between exposures	2 s (reduced FOV)
3. T-range	Limits of temperature coverage	$6.1 < \log T < 7.5$
4. T-resolution	Ability to discriminate temperatures	$\log T = 0.2$
5. X-ray optical resolution	Diameter of 50% enclosed energy	2 arcsec PRF
6. Field of view	Angular coverage of telescope	> 30 arcmin
7. WL Rejection	Reduction of Solar visible light @ focal plane	$> 10^{12}$
8. Data rate	Maximum bit transfer rate out of XRT	2.4 Mb per sec
9. Data volume	Maximum volume per memory fill cycle	60 MB/one orbit
10. Coordination X-ray/WL (Spatial)	Coalign X-ray and WL	One XRT pixel
11. Coordination XRT/SOT (Spatial)	Coalign XRT to SOT	One XRT pixel
12. Coordination XRT/EIS (Spatial)	Coalign XRT to EIS	One XRT pixel

soft X-rays onto a CCD array. Separation between the two is maintained by a stiff, lightweight, low-expansion carbon fiber reinforced polymer (CFRP) tube. The front of the telescope is covered with thin filters to reduce the visible light entering the telescope, and additional filters are positioned in the optical path ahead of the CCD camera, along with a shutter assembly. A focus mechanism allows the camera to be moved ± 1 mm along the optical axis. A visible light optic is included in the center of the X-ray mirror to provide aspect information for the XRT and for the Solar-B mission as a whole. The telescope (i.e., the mirror) is shown schematically in Fig. 2. Its design is discussed in detail in Sec. 3.1.

3.1. MIRROR

Grazing-incidence optics used for soft X-ray imaging generally require a minimum of two surfaces in order to meet the Abbé sine condition that the magnification be constant over the full aperture of the telescope. Wolter used a

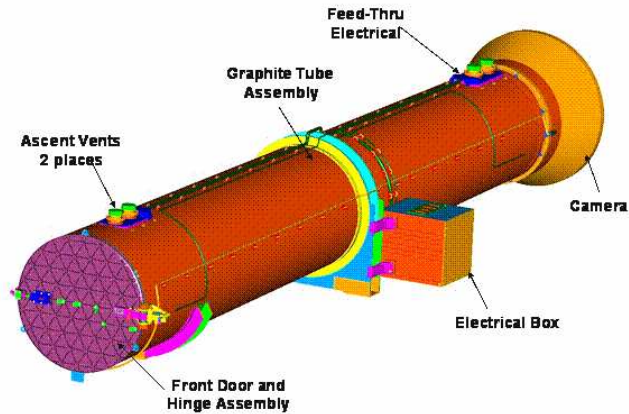


Figure 1. Components of the XRT; the optics are located inside the entrance aperture door.

paraboloid-hyperboloid design, and the more complex Wolter-Schwarzschild design improves image quality slightly by exactly satisfying the condition. Werner Werner (1977) recognized that for a wide-field instrument the field averaged point spread function (PSF) is a better figure of merit to use, and modern computer polishing methods permit the implementation of designs using high order polynomial surfaces which deviate from the more standard conic sections. These designs generally trade on-axis image quality for off-axis improvements. This is acceptable because perfect surfaces cannot be manufactured, so that there is relatively little loss on-axis, whereas the off-axis gain can be considerable. In addition, the detector can be positioned slightly out of focus and thereby achieve a better PSF at finite field angle, at the cost of on-axis performance; this was done, e.g., for the *Yohkoh* SXT (Nariai, 1987; Nariai, 1988; Tsuneta *et al.*, 1991).

The XRT uses a generalized asphere for each mirror element and also has a focus mechanism which allows images to be obtained at the best on-axis (Gaussian) focus and at a range of defocus positions. The image quality as a function of field angle can be varied by changing the location of the camera along the optical axis, as shown in Fig. 3.

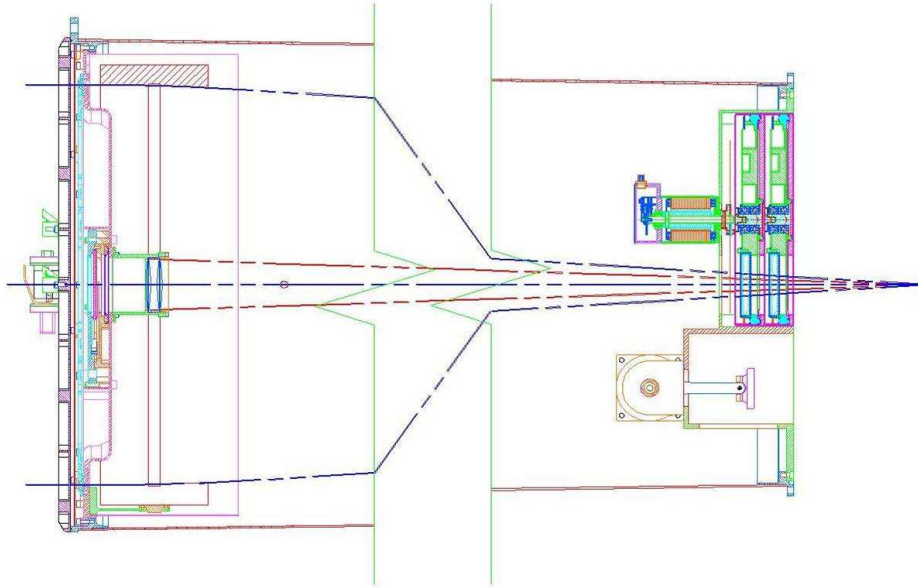


Figure 2. A schematic diagram of the grazing-incidence XRT including the entrance filter assembly and the centrally-located visible light telescope. The GI telescope is shown in section, cross-hatched. The shutter, filter wheel and focus mechanism (U.S. portion) are shown at right. Note that the central part of the CFRP metering tube has been omitted and that the camera is not shown.

3.1.1. *Goodrich Mirror Fabrication*

As-built. The telescope as delivered to SAO met all of the design requirements except for knowledge of the focal length, as shown in Table III. The stated encircled energy diameter requirement was for the optical design itself, while the delivered performance matches the requirement for 2 arcsec imaging.

Table III. As-built XRT Performance Parameters

Parameter	Requirement	As-Built
Optical Design	Single Mirror-Pair	Generalized Asphere
Wavelength Range	6 – 60 Å	Bare Zerodur
Entrance Diameter	341.7±0.1 mm	341.7 mm
Focal Length	2708±2 mm	2707.5 mm
Focus Knowledge	±0.050 mm	±1.4 mm
Field of View	35 arcmin	Optimized over 15 arcmin
Encircled Energy (diameter)	68% @ 0.5 keV 1.57 arcsec	68% @ 0.56 keV 2.3 arcsec
Effective Area	1.0 cm ² @0.53 keV	1.9 cm ²

Performance Predictions. Measurements of the as-built telescope at Goodrich were used to calculate the expected optical performance of the XRT. Fig. 3 shows the predicted as-built RMS point response function (PRF) vs. field angle at different field angles. Comparison with the measured PRF will be presented in Sec. 4 of this paper.

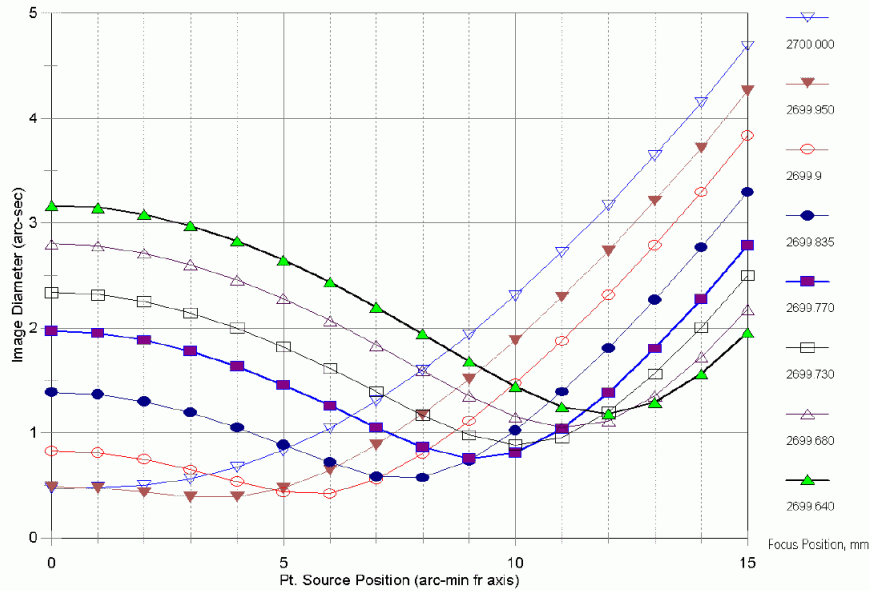


Figure 3. The predicted point response function of the XRT as a function of focal plane location, based on Goodrich measurements of the mirror surface shape.

The size and shape of the PRF are functions of position in the field and of focal plane location along the optical axis. This is illustrated by Fig. 4 (top), which shows the PRF at several off-axis locations for a focal plane located $200\ \mu\text{m}$ ahead of the best Gaussian focus. The corresponding encircled energy plots are shown in Fig. 4 (bottom). These plots are again predictions based on the measurements of the as-built XRT.

The focal length of the XRT (and of grazing-incidence telescopes in general) is dependent on field angle due to focal plane curvature. The predicted values at field angles of 0, 5, 10 and 15 arcminutes are (in mm) : 2707.5, 2707.0, 2706.8 and 2707.2, respectively. The spot centroid for these off-axis point source images is located $\approx 0.78553\ \text{mm/arcmin}$ from the on-axis field center; this quantity is the plate scale.

The measured performance of the XRT will be discussed in Sec. 4 where we present results of the extensive calibration and testing that were carried out at the X-Ray Calibration Facility (XRCF) of the Marshall Space Flight Center.

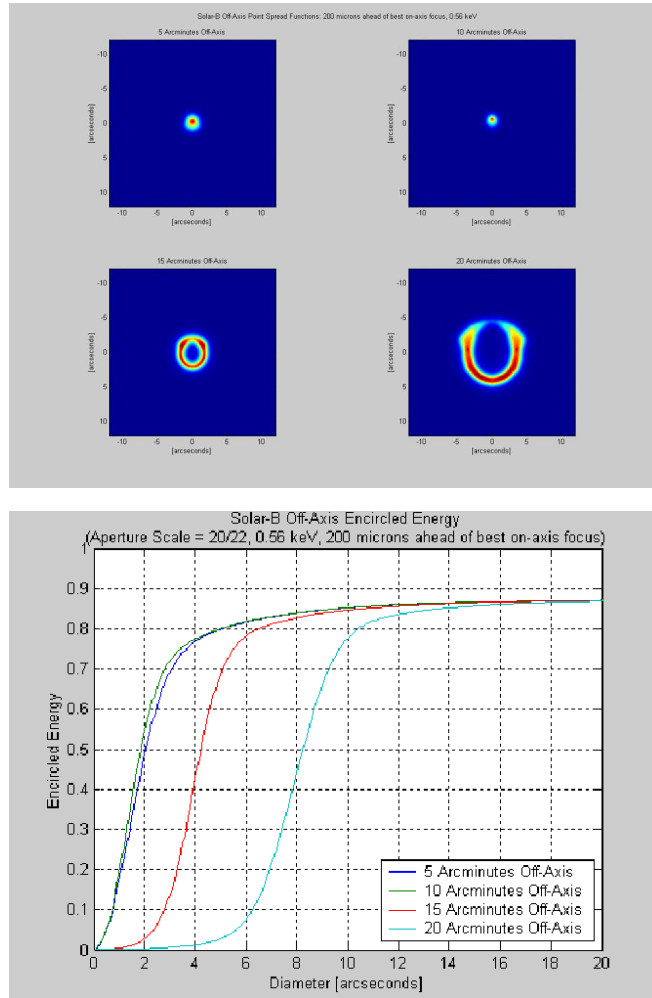


Figure 4. The predicted PRF of the XRT for off-axis angles at a focus position $200\ \mu\text{m}$ forward of best-focus. Top image shows the focal spot and bottom figure shows the corresponding encircled energy curves. (courtesy Goodrich - Danbury)

3.2. FILTERS

The XRT utilizes both entrance aperture prefilters and focal plane analysis filters; these are discussed in the next two sections. We note here that the visible light-blocking requirement for the XRT is 10^{-12} , which translates into a requirement for the prefilter and analysis filters of 10^{-6} each. This requirement determines the minimum acceptable thickness for each filter. It also drives the mechanical design when launch vibration and acoustic loads are taken into account, since the filters must remain light-tight into orbit.



Figure 5. One of the six annular aluminized Polyimide entrance filters of the XRT.

3.2.1. Prefilters

Thin prefilters cover the narrow annular entrance aperture of the XRT. These prefilters serve two main purposes: 1.) to reduce the visible light entering the instrument, and 2.) to reduce the heat load in the instrument.

Taking into account the amount of visible light attenuation needed in order to allow soft X-ray detection at the focal plane CCD, and also taking into account the available methods for reducing visible light entering the telescope, we find that requirement 2. above is automatically met when requirement 1. is met. We will therefore discuss only the first item.

Ideally, the prefilter will reduce the visible light as much as possible and will reduce the X-ray throughput as little as possible. Experience has shown that the material best suited for this purpose is aluminum and we will treat only this choice. However there are several additional factors to consider: Aluminum oxidizes from the moment of manufacture until launch. The rate is strongly affected by humidity, so that handling in dry nitrogen is important. Additionally, Al filters exposed to full Sun in vacuum will become hot. Thermal conduction along the filter to the frame which supports it will cool the filter, and the path length is a major factor in determining the temperature on orbit. Finally, in order to strengthen the filter against launch loads, the aluminum can be mounted on a mesh, on a thin organic film such as Polyimide, or both.

The severity of the vibration and acoustic loads for the Solar-B launch, combined with the availability of thin, strong, highly transmissive Polyimide from the Luxel Corp., determined the choice of substrate thickness. The amount of Al need to provide the required visible light blocking determined the Al

thickness. The XRT entrance filters consist of 1200Å Al and 2500Å of Polyimide, with an estimated 100Å of Al₂O₃. A photo of one entrance filter is provided in Fig. 5.

3.2.2. Focal Plane Analysis Filters

The analysis filters serve two purposes: 1.) to reduce the visible light reaching the focal plane, and 2.) to provide varying X-ray passbands for plasma diagnostics. The analysis filters are held in two filter wheels, operated in series and located in front of the CCD camera, near the focal plane (Fig. 6).

The analysis filters greatly extend the dynamic range of the XRT, differing in thickness by nearly a factor of 10⁴. For faint targets, which also tend to have relatively low temperatures, the thinner filters are used. For flare observations the thickest filters are used. In addition, there is a focal plane filter used with the visible light telescope, which is operated separately from the X-ray channel. This glass filter may also be inserted during X-ray observations in the rare event that the flare intensity exceeds the instrument saturation level.

Inserting the analysis filters into the optical path alters the throughput of the telescope as a function of wavelength. Combined with software that calculates the spectral emissivity of the coronal plasma as a function of its

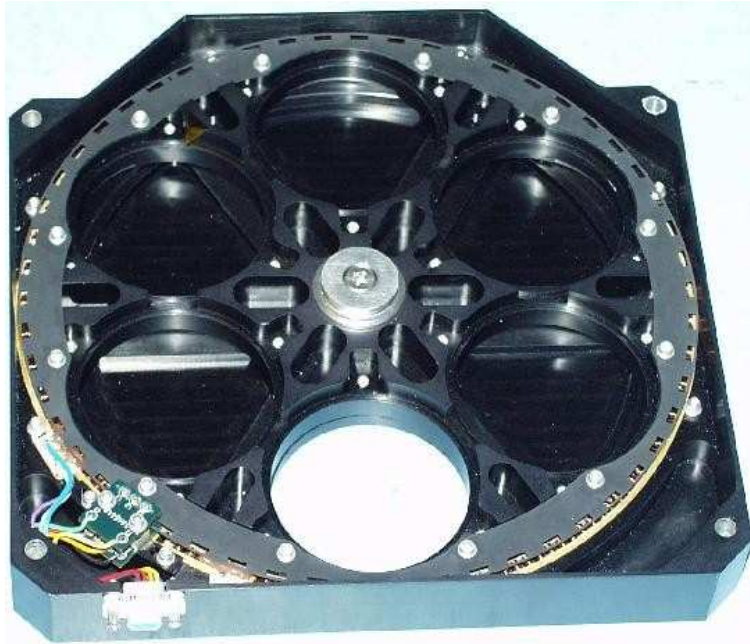


Figure 6. One of the two XRT filter wheels, each of which holds five filters and has one open position.

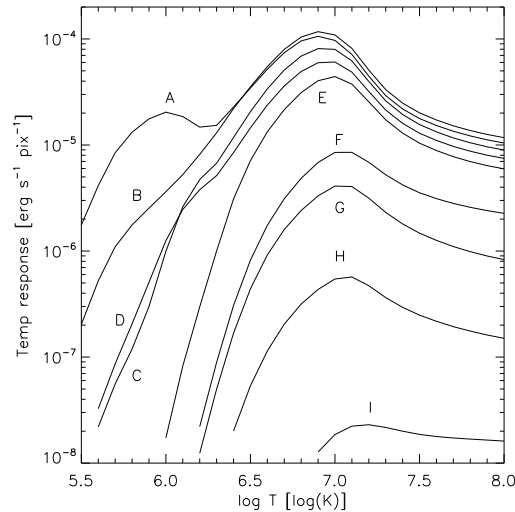


Figure 7. The total XRT temperature response, for all of the X-ray focal-plane filters. Each curve plots the combination of the total instrument response (as $f(\text{wavelength})$) with a coronal plasma emission model (ATOMDB/APEC) for a columnar emission measure of 10^{30} cm^{-5} . The labels indicate which filter is in the path, as follows: A = Al-mesh, B = Al-poly, C = C-poly, D = Ti-poly, E = Be-thin, F = Be-med, G = Al-med, H = Al-thick, and I = Be-thick.

temperature (Smith *et al.*, 2001), we may calculate the response of the XRT for the various analysis filters. This calculation is shown in Fig. 7, in which the throughput of the telescope is shown for an assumed source with constant emission measure (amount of material) as a function of temperature of $1 \times 10^{30} \text{ cm}^{-5}$ over the entire XRT sensitivity range. The units are $\text{erg cm}^{-2} \text{ sec}^{-1}$ at the focal plane, so that the CCD conversion to electrons is not included. These curves represent the basic first step in the quantitative analysis of XRT images; a typical next step might be the type of analysis described in Sec. 5.5 in order to determine the distribution of the EM in a target region of interest.

3.2.3. Filter specification

A summary of the nominal physical properties of the focal plane analysis filters is provided in Table IV. The measured values for the component thicknesses are discussed in the next section.

3.2.4. Palermo Testing

Several of the flight focal plane filters for the XRT were tested at the X-Ray Astronomy Calibration and Testing (XACT) facility of INAF-Osservatorio Astronomica di Palermo. The goal of these calibrations was to determine the spatial uniformity of the filters and the transmission properties (Barbera *et al.*, 2004). Of the nine filters tested seven are installed in the XRT. The results show that the spatial uniformity is 2% or better for the metal on Polyimide

Table IV. Physical Characteristics of the XRT Focal Plane Analysis Filters.

Analysis Filter Characteristics						
Filter ID	Material	(Å)	Filter	Support	Oxide	(Total, Å)
A. Al-mesh	Al	1600	–	82%	Al ₂ O ₃	150
B. Al-poly	Al	1250	Polyimide	2500	Al ₂ O ₃	100
C. C-poly	C	6000	Polyimide	2500	N/A	N/A
D. Ti-poly	Ti	3000	Polyimide	2300	TiO ₂	100
E. Be-thin	Be	9E4	N/A	N/A	BeO	150
F. Al-med	Al	1.25E5	N/A	N/A	Al ₂ O ₃	150
G. Be-med	Be	3.0E5	N/A	N/A	BeO	150
H. Al-thick	Al	2.5E5	N/A	N/A	Al ₂ O ₃	150
I. Be-thick	Be	3.0E6	N/A	N/A	BeO	150

filters and better than 3.3% for the single metal filters. The transmission tests showed that the results were within 5-10% of the predicted values.

After launch of the XRT the witness samples for the flight filters (entrance and focal plane) will be measured for transmission at the XACT. This will provide the final transmission calibrations.

3.2.5. XRCF Testing

The transmissions of the focal plane filters listed in Table IV were also measured during the End-to-End test at the XRCF. The measured transmissions are within 5-20% of the predicted values for all of the exposures with a high photon flux. Table VI shows the sources that we had available to us for these tests, and Table VII shows the comparison of measured and predicted transmissions.

3.3. SHUTTER

The focal plane shutter used in the XRT is a modified version of the TRACE shutter (Fig. 8). It can be operated in two modes: a continuous sweep at fixed rotation speed, or a start-stop mode in which the large opening is brought into the path and kept there for the desired length of time. The narrow openings may be employed in a multiple-pass mode, so that a large set of exposure times can be generated. The set of exposure times chosen for initial operations is given in Table V.

3.4. WL TELESCOPE

The XRT includes a visible-light imager coaxial and confocal with the X-ray telescope. It is a simple achromat designed to image the Sun in the 400–500 nm band with 2 arcsecond spatial resolution. The lens materials, fused silica

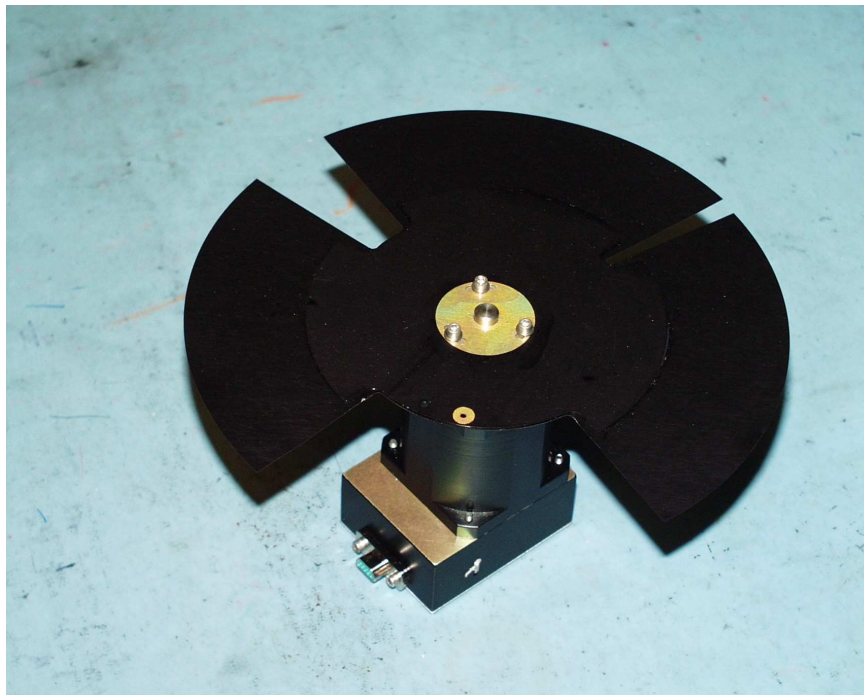


Figure 8. The XRT shutter is a thin rotating blade with two narrow slits for 1 ms and 8 ms exposures, plus a slot for exposure times ≥ 44 ms.

and SF16, are chosen for their insensitivity to radiation darkening, and are used to correct axial color between 405 and 495 nm; the design also corrects for spherical aberration at 430 nm.

The nominal focal length of the doublet is 2705 mm, and the aperture is 50 mm, giving an f-number of f/54. The optic is mounted in a manner that permits adjustment along the optical axis so that the visible-light focal plane is positioned coincident with the as-built X-ray focal plane, to within the depth of focus of the XRT. The WL depth of focus is substantially larger than the XRT's.

The WL Telescope is fitted with an entrance aperture filter manufactured by the Andover Corporation and having a passband centered on the G-band at 430.7 nm with a FWHM of 18.9 nm. A similar filter is placed in one of the focal plane filter wheels, with a tested central wavelength of 430.3 nm and FWHM of 17.7 nm. The peak transmissions of the filters are 49.3% and 29.6%, respectively, including a built-in neutral density coating on the focal plane filter for off-band rejection. The additional neutral density filter, of ND=1.3, was selected to provide a nominal exposure time of 1/100 second. The correct ND value was chosen by calibrating the WL Telescope

Table V. Initial Table of Available XRT Exposure Values.

Available XRT Exposure Times.

ID#	τ_{exp} (sec)	ID#	τ_{exp} (sec)
0	0.001	18	0.71
1	0.002	19	1.00
2	0.003	20	1.41
3	0.004	21	2.00
4	0.005	22	2.83
5	0.008	23	4.00
6	0.012	24	5.66
7	0.016	25	8.00
8	0.024	26	11.3
9	0.032	27	16.0
10	0.044	28	22.6
11	0.063	29	32.0
12	0.086	30	45.2
13	0.125	31	64.0
14	0.177	32	64.0
15	0.250	33	64.0
16	0.354	34	64.0
17	0.500	35	64.0

at Williams College using their 0.6 m solar telescope and obtaining images at varying elevations, so that an extrapolation to zero air mass could be obtained.

3.5. VISIBLE LIGHT IMAGER AND X-RAY TELESCOPE CONFOCALITY

The XRT and VLI share a CCD camera and a focus mechanism that has a range of motion of ± 1 mm. Therefore, in order to achieve the required optical performance, it is necessary that their respective best on-axis focus positions both lie within the range of the focus mechanism. In order to reasonably minimize cadences and the frequency of mechanism motions, it is desirable that the best on-axis focus position for the VLI lie within 250 microns of that for the XRT. This value is substantially smaller than the depth of focus of the VLI, so that refocusing in switching from XRT to VLI would not be needed.

Observations were taken at the XRCF of a visible light penray lamp at the same distance along the facility axis as the X-ray source. Measurements were taken across the range of focus mechanism positions, with the VLI shutter in both the open and closed states. At this point in the End-to-End test, the telescope configuration included a spacer to account for the finite

source distance and the consequent shift in location of the focal plane image. The prefilters were not included, so that images taken with the VLI shutter open registered light traversing both the XRT and VLI optic. Images taken with the VLI shutter closed registered light traversing the XRT optic. In order to isolate an image focused solely by the VLI optic, each closed image is subtracted from its corresponding open image. This subtraction also compensates for dark current in the image.

The images of the visible light source were fitted with a 2D Gaussian model, which is valid for focus positions near best focus. The RSS Gaussian widths are then plotted as a function of focus position (Fig. 9). The best on-axis focus position is defined to be where the RSS Gaussian width is a minimum. However, analysis indicates that, over the range of motions available in the XRT, the data are well-fit with a horizontal straight line. This result corresponds to an instrument that has a broad depth of focus, in which case all (on-axis) focus positions produce images with equivalent focus. Note that the size of the spot includes the finite size of the lamp used to produce the WL image at the XRCF.

The VLI data are consistent with the prediction that it would have a depth of focus (2.2 mm) broader than the range of motion of the focus mechanism (1.0 mm). Therefore, any VLI focus position within 250 microns (\approx 500 steps in the diagram) of the XRT best focus position at -313 microns will give acceptable focus of the VLI.

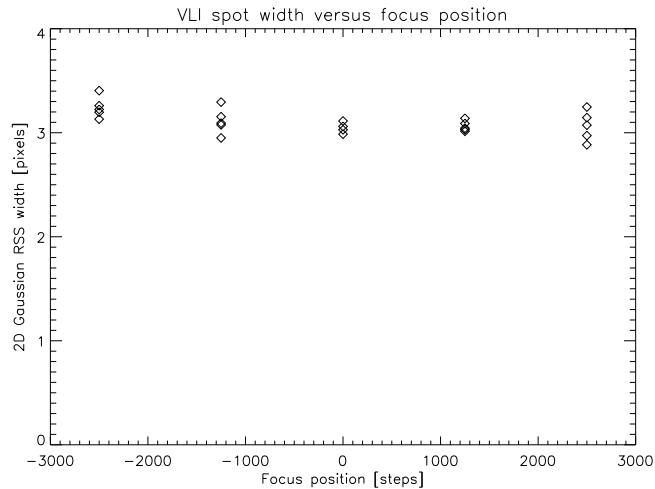


Figure 9. The spot size of a visible-light source imaged through the visible light imager (VLI) as a function of distance along the optical axis of the XRT.

3.6. VISIBLE LIGHT IMAGER AND X-RAY TELESCOPE CO-ALIGNMENT

The visible light source was placed adjacent to the X-ray source at the same horizontal distance (530.6 m) from the front of the XRT instrument along the facility axis, but laterally offset by 14.1 cm.

For the X-ray measurements, the Cu-L source was used. Normal images were taken at the Best Focus position, and the XRO peak flux centroids were located to ± 0.5 arcseconds, i.e. one pixel on the CCD. For the VLI measurements, normal images were taken at the nominal 430.5 nm focus position, and the VL peak flux centroids were also located to ± 0.5 arcsecond.

The measured offset between the XRT and VLI centroids was corrected for the physical offset of the sources and an estimate of the error in the measure of the offset. The VLI and XRT axes net alignment offset is 17.0 ± 5.0 arcseconds, with the uncertainty dominated by the $\sim 1/4''$ uncertainty in the location of the visible light source. This alignment accuracy is well within the required coalignment tolerance of one arcminute. The tighter requirement on *knowledge* of the coalignment will be determined after launch during the commissioning phase of the satellite.

4. XRT Mirror Imaging Performance

Two major test sequences of the XRT were carried out at NASA's XRCF. In the first (mirror calibration test), the imaging properties such as point response function, effective area as a function of wavelength and off-axis response of the XRT were determined. The XRT was then returned to the XRCF after assembly into flight configuration, specifically to establish the focal length via an end-to-end test. Image performance data from both the mirror calibration and end-to-end test are presented in this section. The total telescope throughput is discussed in the following section. Details of the CCD camera calibration are discussed in the companion XRT camera paper in this volume.

4.1. TEST PLAN.

The XRCF consists of an X-ray source located at one end of a 518 m vacuum pipe, with a large vacuum chamber at the other end of the pipe to hold the test article and associated test equipment. Our tests used an Electron Impact Point Source, in which an electron beam is focussed onto a target, at a voltage chosen to excite a characteristic line; typically K- α or L- α lines are chosen, for strength and spectral purity. A thin metallic filter, usually of the same material as the target is then placed in the path to filter out unwanted X-ray energies while permitting the characteristic X-rays to pass. The primary lines used in this test are listed in Table VI. The mirror calibration tests carried out were:

Table VI. Available X-ray lines for the XRT Calibration at the XRCF.

Line	Energy (keV)	Wavelength (Å)
C-K	0.277	44.7
O-K	0.525	23.6
Cu-L	0.933	13.3
Al-K	1.49	8.3
Mo-L	2.29	5.4

Focus determination The mirror is aligned with the source-detector line. A scan through the focus range was performed and 2-D Gaussian curve fits were applied to images. The best on-axis focus (BF) was located by the minimum in the polynomial fit of the RSS sigma width values for the FWHM. The focus position that provides the best average imaging across the field of view (FOV) is called the FOV Optimized Focus (OF), defined as the position where the on-axis FWHM is equal to 2". This yields the largest extent of field angles meeting the resolution requirement.

On-axis PSF and encircled energy Characterization of the performance of the XRT mirror was performed after completion of the optical axis alignment of the mirror to the X-ray beam. Data was collected using the Cu-L source using both the CCD and proportional counters. The combination of these data was used to find the PSF and encircled energy.

On-axis effective area A flow proportional counter (FPC) with a wide pinhole aperture was used to alternately measure the photon count rate through the effective area of the X-ray optic and through the unobstructed visible light aperture along the same optical axis. The ratio of the on-axis effective area to the calibrated pinhole aperture area is equal to the ratio of the photon count rate through the respective areas. Independent measurements of the source flux rate provided normalization against time variations. Proportional counter data were taken with the five different energy sources (Table VI).

Off-axis PSF and encircled energy This test was performed with the Cu-L (0.933 keV) source, using an off-axis configuration of 15.6 arcminutes. The X-ray beam center was measured with an FPC and an array of calibrated pinhole apertures from 20 μm to 20 mm. These data were used to

characterize both the off-axis PSF and encircled energy performance of the XRT optic.

Off-axis effective area The XRT off-axis effective area was measured at an angular displacement of 15.6 arcminutes (immediately subsequent to the off-axis PSF measurements). The 20 mm pinhole aperture and an FPC detector were used to sample the beam center for both the Cu-L (0.933 keV) and O-K (0.525 keV) X-ray sources, in conjunction with measurements through the VLI. In other respects, the test procedure was identical to that described for the on-axis effective area measurements.

Wings of the PSF To determine the contribution of the wings of the PSF, 89 normal and dark images were collected at best on-axis focus. A subset of these images were calibrated and summed. Fluxes within annuli approximately 3 CCD pixels thick were summed with the midpoint radius of each annulus expanding toward the edge of the CCD in discrete steps of 3 CCD pixels.

Thermal response of the telescope Images were collected at three different chamber temperature configurations: 15°C, 22°C, and with a 1°C temperature gradient around the mirror circumference.

4.2. BEST ON-AXIS FOCUS PSF

The BF was found as described above. During the mirror calibration tests, data involving sub-pixel motions were collected to help determine the azimuthal location of best focus. In this procedure, images were taken after the CCD position was shifted 7 microns ($\approx 1/2$ pixel) in both the \hat{z} and the \hat{y} directions. An estimate of the point spread function (PSF) was derived from these data via an interpolation method (Fig 10), after which corrections for the finite source distance and the effect of gravity were applied in order to derive the PSF as it will appear in flight configuration (Fig 11).

After constructing the PSF, annuli of successively increasing inner radii were formed, with the peak of the PSF taken as the origin of all of the annuli. The fluxes contained within these 2-pixel thick annuli were summed and plotted as a function of diameter of the annuli. The resulting plot is shown as one of the curves in Fig. 12. This plot shows that the mirror meets the NASA requirement that 50% of the encircled energy be contained within a diameter of 27 microns (2 arcsec).

The PSF was also measured via a series of pinholes positioned on axis at the plane of best focus, with a proportional counter located behind the pinholes. These measurements confirmed the size and shape of the inner core of the PRF, and were also used to measure the large-angle wings of the PRF; those results are presented in Sec. 4.3.

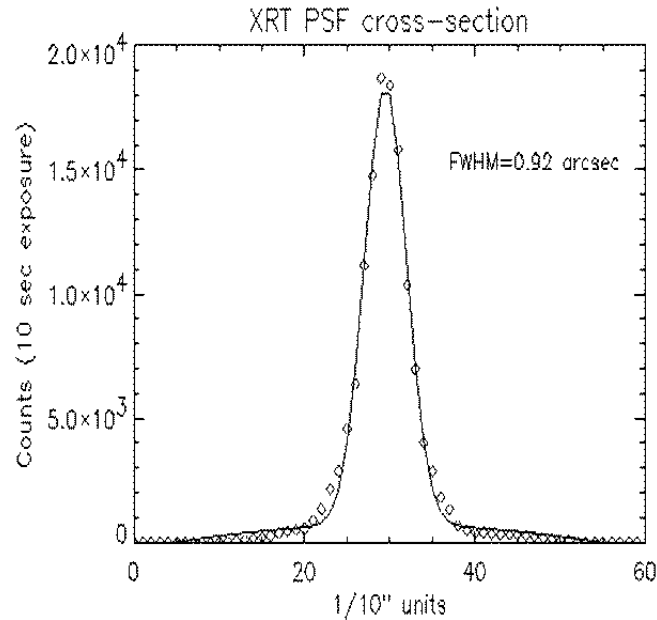


Figure 10. The PRF of the XRT before correction for the finite source distance during XRCF testing and for the deformations due to gravity. The FWHM is less than one XRT CCD pixel.

The PSF as measured contains two contributions which are not present on-orbit: the XRCF source is of necessity located at a finite distance from the telescope, and the optic is distorted due to the effect of gravity. We have modelled both of these effects and corrected the measured PSF, with the result shown in Fig 11.

Mirror contribution. The experimentally-determined encircled energy function of the XRT is shown in Fig. 12, which compares the prediction with two measurements, one using a CCD and one using a nested sequence of pinholes. The only discrepant data point is that using the large ($50 \mu\text{m}$) pinhole; this is being investigated. The CCD contribution to the instrument PRF is discussed in the companion paper in this volume.

4.2.1. Performance across the FOV

Images taken at Cu-L (0.933 keV) across the field of view of the XRT are used to determine the PSF when the camera is positioned at the plane of best focus. The results are summarized and compared to a curve showing the variation in RMS spot size vs. field angle obtained using a ray trace program which takes the measured telescope surface figure. Comparison of the spot

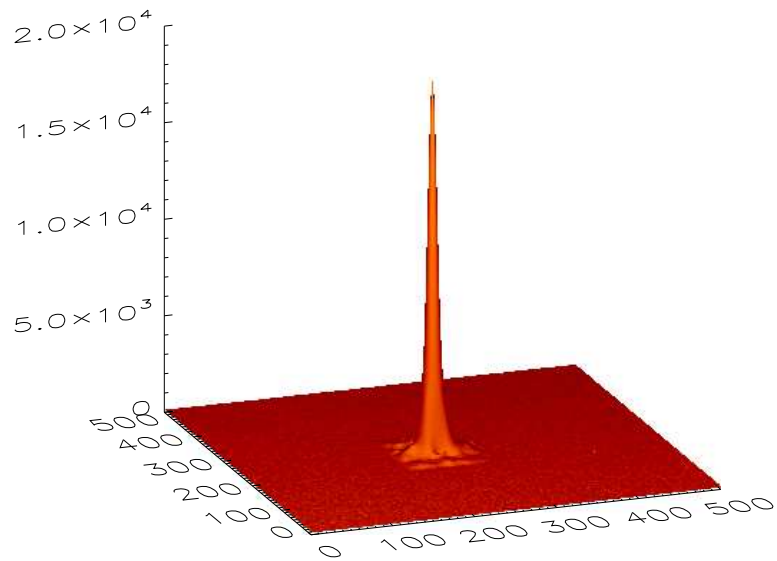


Figure 11. The PRF of the XRT corrected for the finite source distance during XRCF testing and for the deformations due to gravity. The FWHM is ~ 0.8 arcsec, less than one XRT CCD pixel.

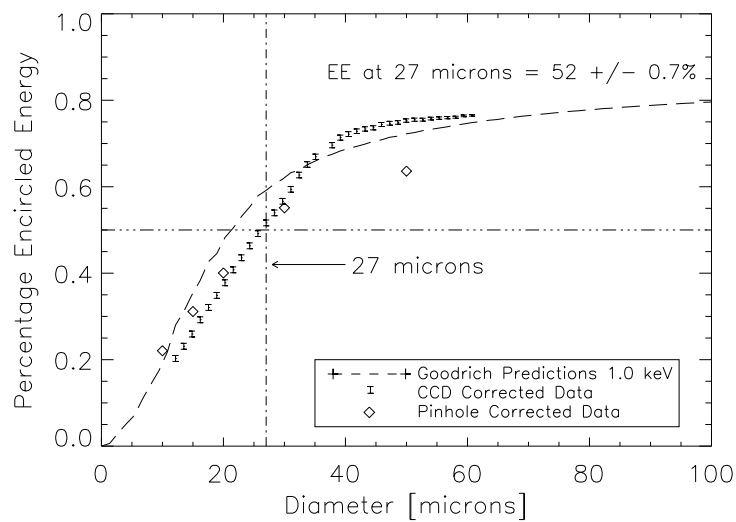


Figure 12. The predicted vs. measured encircled energy function of the XRT for the on-axis Gaussian focus position. Dashed line is the Goodrich prediction and the diamonds and brackets indicate the experimental values.

size data obtained at the XRCF after finding the location of best focus to the predictions is shown (Fig. 13). We find excellent agreement between the predicted performance and the measured values.

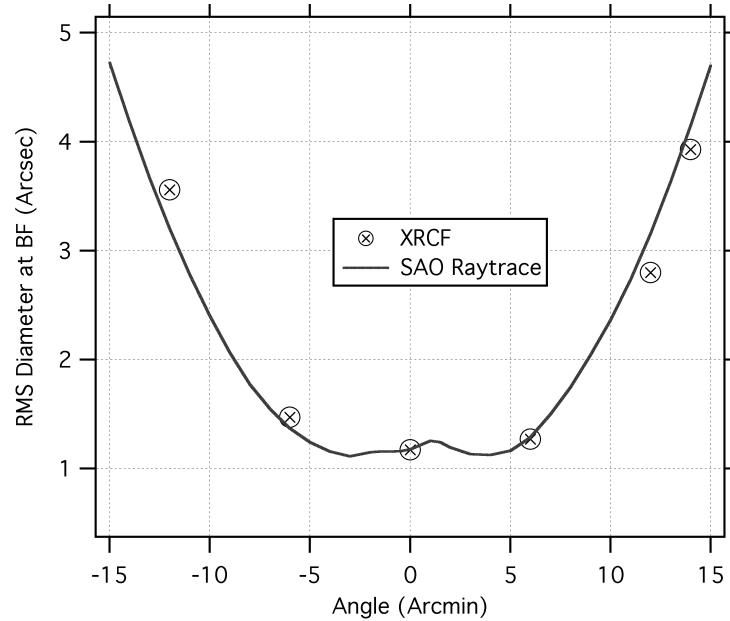


Figure 13. The measured vs. predicted off-axis spot size in test configuration, i.e. without the 1G and finite source distance corrections.

4.3. WINGS AND SCATTERING

The wing response is defined as the ratio of the off-axis flux to the on-axis flux for a point source. The off-axis angle must also be specified and for the XRT the requirement was specified for an annular ring of width 1 arcsec located at a radius of 60 arcsec. The wing response was measured at the XRCF for the full range of angles from 0 to slightly more than 60 arcsec using the CCD images for the bright inner portion of the PSF and the pinhole measurements for the faint outer portion. Ten long-exposure CCD images were averaged for the core determination and the result was spliced onto the pinhole data in their overlap region. The wing response of the XRT PSF (Fig. 14) was sampled with an FPC using 100 and 300 micron calibrated pinhole apertures, at a range of positions between 0 and 1000 microns from the core center. A 2D Lorentzian model was fit to this dataset. The PSF core was sampled with an FPC using a 10 micron pinhole, in a 7×7 array of positions within 22 microns of the core center. A 2D Gaussian model was fit to this latter dataset. The Gaussian core and Lorentzian wing models were matched at 13 microns, and together normalized to the core peak value. The measurements show that the scattering is $< 10^{-5}$ at 1 arcmin off-axis, at an energy of 0.93 keV.

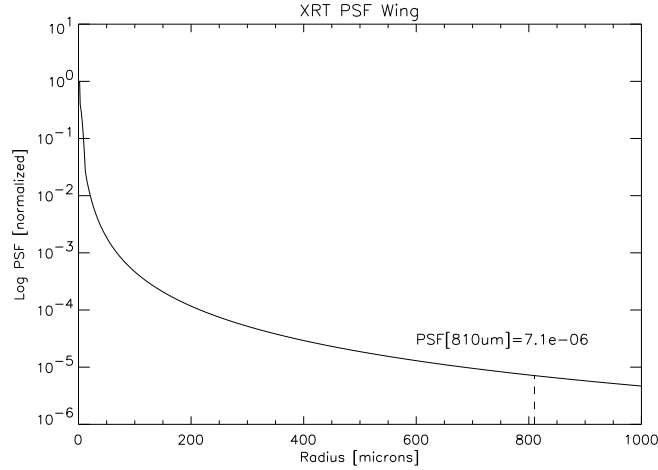


Figure 14. The wing response of the XRT PSF at a range of positions between 0 and 1000 microns from the core center. A 2D Lorentzian model was fit to this dataset; see text for details.

5. Throughput

5.1. MIRROR EFFECTIVE AREA

The effective area of the XRT depends upon the geometric area and the reflectance of the mirror surfaces. The latter quantity is wavelength-dependent and enters twice because the XRT is a two-bounce telescope. The predicted effective area agrees well with the measured area, as shown in Fig. 15. The effective area at an off-axis angle of 15.6 arcminutes was also measured, as shown on the figure; the lower reflectance indicates the degree of vignetting at this angle. The overall XRT response also includes the entrance filter and the focal plane analysis filter transmissions, and the CCD efficiency.

5.2. FILTER TRANSMISSION

As a check on the thickness of the analysis filters, their transmission at X-ray wavelengths was tested at the XACT facility in Palermo using the same set of emission lines which are available for the XRCF testing; the energies associated with these emission lines were shown in Table VI.

The results of the measurements are shown in Table VII. The uncertainties in the measured transmissions are dominated by counting statistics. For some of the thick filters measured with the weaker emission lines, the time available for testing determined the number of photons which could be collected, so that the error bars are relatively large. We see that, to within the measurement uncertainties, there is acceptable agreement in all cases between the predicted and the measured values.

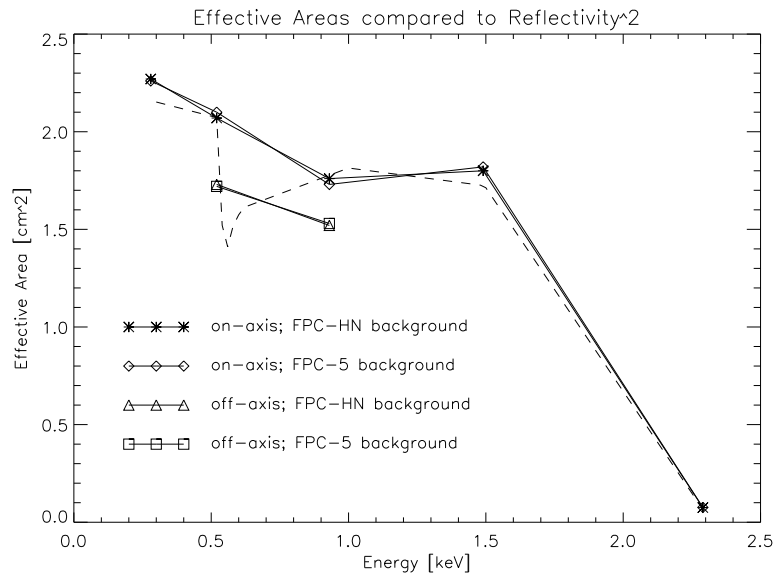


Figure 15. The effective area of the XRT optic as a function of energy, both on- and off-axis. The predicted on-axis areas for two reflections on the mirror (dashed line) are consistent with the on-axis measurements (asterisks and diamonds on solid lines). Off-axis measurements are also shown (triangles and squares on solid lines) for a field angle of 15.6 arcminutes.

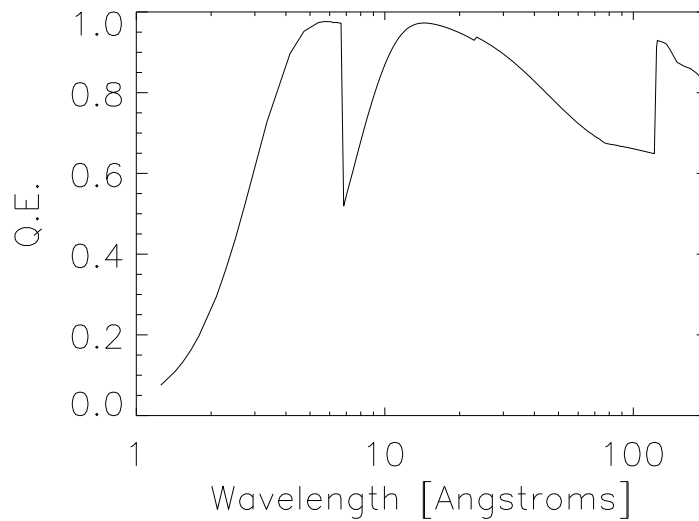


Figure 16. The nominal quantum efficiency curve for the XRT CCD camera, shown here for illustrative purposes only.

Table VII. Analysis Filter Measured (upper) vs Predicted (lower) Transmissivities.

Emission Line:	C-K	O-K	Cu-L	Al-K	Mo-L
Energy (keV):	0.227	0.525	0.933	1.49	2.5
<i>Filter</i>	<i>Measured Transmission \pm Uncertainty</i>				
	<i>Predicted Transmission</i>				
Al-mesh	23.8 \pm 6.9	80.8 \pm 8.5	93.7 \pm 6.2	94.5 \pm 5.2	77.4 \pm 7.0
	21.2	72.1	91.9	97.6	92.0
Al-poly	24.0 \pm 8.3	51.5 \pm 8.6	77.4 \pm 7.0	94.5 \pm 5.2	89.6 \pm 7.3
	19.4	50.3	82.0	94.6	91.2
C-poly	64.1 \pm 5.5	7.9 \pm 4.8	60.6 \pm 4.8	79.2 \pm 3.0	94.1 \pm 7.0
	65.3	10.0	57.9	86.3	95.6
Ti-poly	41.8 \pm 7.2	5.5 \pm 3.2	33.9 \pm 3.1	68.8 \pm 4.4	91.0 \pm 6.4
	34.0	3.1	33.0	71.7	89.3
Be-thin	5.6	—	26.1 \pm 3.5	77.8 \pm 5.6	90.7 \pm 6.6
	0.0	0.1	27.8	72.6	91.1
Be-med	6.8	—	4.5 \pm 2.7	48.9 \pm 6.8	77.2 \pm 5.3
	0.0	0.0	1.5	32.6	73.7
Al-med	—	—	2.3 \pm 1.7	22.6 \pm 4.4	2.5 \pm 1.9
	0.0	0.0	0.6	23.6	0.2
Al-thick	—	—	—	5.1 \pm 2.1	—
	0.0	0.0	0.0	6.0	0.0
Be-thick	—	—	—	—	7.8 \pm 2.9
	0.0	0.0	0.0	0.0	6.7

5.3. CCD QE

The calibration of the XRT camera is described in detail in a companion paper in this volume. For reference purposes we provide a calibration curve here, Fig. 16, since this is part of the throughput calculation for the XRT instrument as a whole.

5.4. TOTAL TELESCOPE THROUGHPUT

The total throughput is the convolution of all relevant terms, including pre-filter transmission, mirror effective area, analysis filter transmission and CCD quantum efficiency. These contributions are summarized as an effective area, and the curves for all of the nine XRT filter channels are shown in Fig. 17.

5.5. DEM ANALYSIS

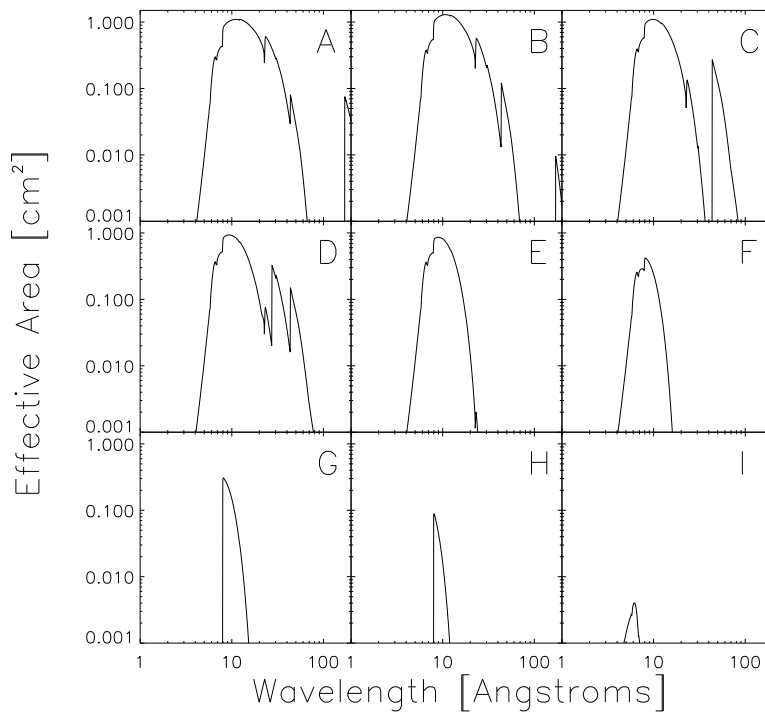


Figure 17. The total telescope throughput of the XRT for each of the nine X-ray filter channels. The labels indicate the filter channels as follows: A = Al-mesh, B = Al-poly, C = C-poly, D = Ti-poly, E = Be-thin, F = Be-med, G = Al-med, H = Al-thick, and I = Be-thick.

The next step after one is able to see the coronal structures is to determine their physical basic properties. Among these is the measurement of the amount of material present in the corona as a function of temperature – the differential emission measure, or DEM. The procedure we use for finding the best-fitting DEM for a given set of observations in several spectral channels has been described in Weber *et al.* (2004). We consider a set of images

taken of an active region (AR), and we estimate the DEM in a given pixel. Our procedure then produces an iterative least-squares fit to the observations using a DEM represented by a spline with evenly spaced knots in $\log(T_e)$ space. With the forward modeling approach, we assume a differential emission measure and compare the predicted observations for each filter with the real observations, iterating the DEM until an acceptable fit is found.

The corona is known to be highly inhomogeneous in temperature, density, and magnetic field – the isothermal approximation is often inadequate for describing the optically thin solar atmosphere across length scales comparable to the span of an XRT pixel. The actual DEM distribution in an active region is thus expected to include material across a wide temperature range. We analyzed our DEM procedure using a realistic DEM model that is included in the CHIANTI database in order to evaluate the methods employed and to establish the number of observing channels needed in order to reproduce the input data. There is, in principle, no limit to the complexity of the model DEM which could be chosen. However, the physics of the situation – primarily the Boltzmann width of the spectral lines, causing them to be formed over a fairly wide temperature range in the corona – provides a fundamental limitation to the resolving power of any spectroscopic analysis (Craig and Brown, 1976). The amount of structure present in this model is reasonable for these tests.

Figs. 18a and 18b suggest how well the input DEM can be reconstructed as a function of the number of observing channels used. In Fig. 18a, four XRT channels have been used to perform fits. The figure shows the model AR DEM (solid line with two humps), the distribution of fitted DEMs (grayscale), and the median values of the 100 DEM runs (diamonds). The DEM is fitted over the log temperature range 5.5–8.0 and 3% noise is assumed. These relatively high-T XRT filter channels determine the presence of the hotter peak of material, as indicated by the convergence of the median fit to the model DEM curve, but fail to detect the cooler material. The narrow uncertainty bands indicate that the fits are robust or, in the words of one author, “reliably bad”.

In Fig. 18b, the same model is fitted with seven channels; that is, we have included thinner filters in the analysis. It is obvious that the fitted DEMs more accurately reproduce the model DEM curve across the entire temperature range. Even though the uncertainty bands are not as constrained as in Fig. 18a, they adequately indicate the presence and temperature of the cool component. To achieve good results in DEM reconstruction with XRT data, it is thus important to have observations in many (independent) channels.

The Number of Channels. The physics of ionization fraction formation under coronal conditions combined with the range of temperatures found in the corona leads to a definite requirement on the number of independent channels that need to be recorded in order to reconstruct the emission measure distribu-

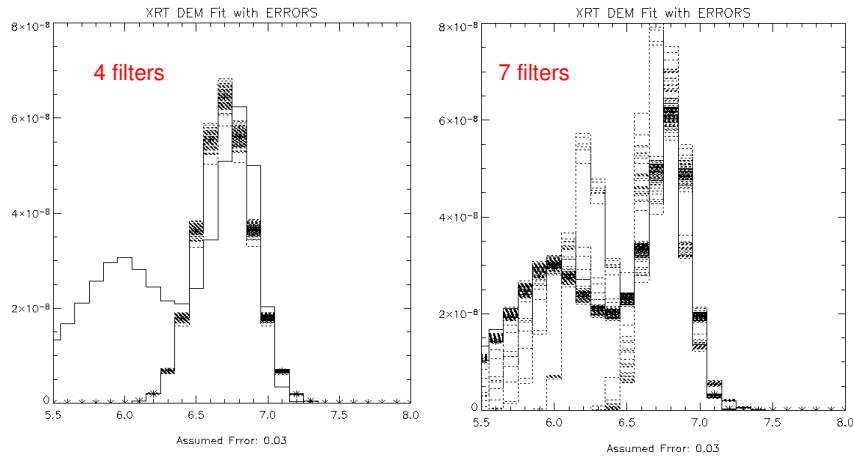


Figure 18. Two attempts at reconstructing an input model (solid histogram) of the DEM from a solar active region: a) at left, uses four XRT channels and produces a poor fit, b) at right, uses seven channels and yields an acceptable fit. Each panel shows 100 runs, with noise added for realism.

tion. The narrowness of the temperature range over which a typical ionization state is formed in the corona, combined with the requirement to have complete but non-redundant coverage, means that at least six channels must be used. This is shown explicitly in Fig. 18, where we examine how the removal of even a single channel affects the quality of the DEM reconstruction for a typical active region.

DEM reconstruction thus requires observations in at least six independent channels, most of which should record a useful number of counts. This is the major reason for the choice of up to nine channels, spanning a large temperature range, in the XRT.

This analysis indicates that DEM determinations are data-intensive, since they require that a large number of channels be used. Because telemetry is limited, as is onboard storage, and because some scientific objectives require high cadence (i.e., the use of a single channel or a small number of channels), the multi-channel DEM programs will need to be specifically scheduled when needed.

6. Conclusions

The X-ray telescope for Solar-B will be the highest resolution solar X-ray telescope ever flown. The optical design and mirror quality ensure excellent

imaging performance across the FOV and low scattering from bright flaring regions. In combination with the observations from the SOT and EIS, the XRT's broad temperature response, large dynamic range and high throughput will achieve breakthrough science in the areas of CMEs (onset, coronal magnetic field structure), coronal heating (loop temperature dynamics, waves, loop-loop interactions), flares, reconnection and jets (the role of magnetic topology, energetics) and the relationship of the photospheric magnetic field evolution to coronal dynamics.

Acknowledgements

The U.S. portions of the XRT program are supported by contract NAS8-01003 from NASA to the Smithsonian Institution. We would like to thank Larry Hill and his staff at MSFC for effective and helpful management of this program, and John Davis of MSFC for his experienced and useful advice and suggestions. We thank J. Pasachoff and the staff at Williams College for assistance with the VLI calibration. We also thank the staff at Goodrich (Danbury) for their effort and skill in fabricating the X-ray telescope and for permission to use the mirror performance figures.

References

- Barbera, M. *et al.*: 2004, *Proc. SPIE* **5488**, p. 423.
 Craig, I.J.D. and Brown, J.C.: 1976, *Astron. & Astrophys.* **49**, 239.
 DeLuca, E. *et al.*: 2005, *Adv. Space Res.* **36**, 1489.
 Golub, L.: 2003, *Rev. Sci. Instr.* **74**, 4583.
 Nariai, K.: 1987, *Applied Optics* **26**, 4428.
 Nariai, K.: 1988, *Applied Optics* **27**, 345.
 Smith, R.K., Brickhouse, N.N., Liedahl, D.A. and Raymond, J.C.: 2001, *Astrophys. J.* **556**, L91.
 Tsuneta, S. *et al.*: 1991, *Solar Phys.* **136**, 37.
 Weber, M.A., DeLuca, E.E., Golub, L. and Sette, A.L.: 2004, *Proc. IAU Symp.* 223, *Multi-Wavelength Investigations of Solar Activity*, p. 321.
 Werner, W.: 1977, *Applied Optics* **3**, 764.